Chapter 7
Disentangling of Stellar Spectra

Petr Hadrava

7.1 Introduction

Observations and the corresponding theory of binary and multiple stars provide us with a clue to the physics of stars and hence also to the universe beyond the Solar system:

- From observations of a **visual binary**, we can determine its orbital period P, inclination i, eccentricity e and periastron longitude ω, the angular distance α between the components (and hence the ratio of the semi-major axis a to the distance d of the system) and light ratio L_1/L_2 of the components.
- From observations of an **eclipsing binary**, we can also assess P, i, with some limitations also e and ω, and in addition to L_1/L_2 also the ratios of the components' radii $R_{1,2}$ to a.
- From observations of Doppler shifts of lines in spectra of **spectroscopic binaries** we can also obtain P, e and ω. Moreover, we can get the semi-amplitudes of radial-velocity curves $K_{1,2}$, i.e. for a reasonable estimate of i we know the orbital velocities $v_{1,2}$ and we can calculate the absolute size of a and also the masses $M_{1,2}$ of the component stars.

For spectroscopic binaries which are simultaneously eclipsing, we can thus determine the basic physical parameters of the stars – $M_{1,2}$ and $R_{1,2}$, and from colour photometry or spectroscopy also the temperatures $T_{\mathrm{eff}1,2}$ and hence the luminosities $L_{1,2}$ of the component stars and the photometric distance d of the system. From these data, we can calculate the angular separation α, including for stars that we cannot resolve by direct imaging (e.g., $\alpha \leq 0.2\,\mu$ as for the first binary measured in M31 [15]).

P. Hadrava (✉)
Astronomical Institute, Academy of Sciences, Boční II 1401, Praha 4, Czech Republic
e-mail: had@sunstel.asu.cas.cz

H.M.J. Boffin et al. (eds.), *Astronomy at High Angular Resolution*, Astrophysics and Space Science Library 439, DOI 10.1007/978-3-319-39739-9_7

However, the goal of indirect imaging which is usually dependent on some theoretical model of the object (e.g., in this case the model of components radiation and the interstellar absorption) is not to compete with observational techniques of direct imaging, not to say to replace them. To the contrary, the improvement of such techniques is even more desirable in connection with indirect imaging because they may provide a complementary information enabling to verify the theory and to improve the underlying assumptions. For instance, until recently, there were practically no binaries observed as both visual and spectroscopic because the former technique prefers wide orbits while the former close binaries with higher amplitudes of radial velocities. Interferometry, however, enables higher angular resolution, while improved spectroscopic instrumentation and data processing provides better spectral resolution, so that the overlap of these two sets of techniques increases. From a combination of interferometric and spectroscopic observations of (even non-eclipsing) binaries we can determine α, i, $v_{1,2}$, a and hence also the geometric distance d (e.g., [23], which solved the Pleiades distance controversy caused by an error in Hipparcos results).

The observations of binaries can thus provide us with more information than those of single stars, but their interpretation is at the same time more difficult. In particular, the spectra (as well as the colours) of the component stars are blended and can only be distinguished by taking into account their variations with the orbital motion. While for single stars it is usually sufficient to fit their observed spectra with synthetic spectra parameterised with $T_{\rm eff}$, $\log g$ (the surface gravity) and abundances of elements X_i, the physics of binaries is more complicated due to their interaction and proximity effects, such as tidal forces or reflection effects. More sophisticated theoretical tools and data-processing methods are thus needed to interpret the observational data. Such methods actually reveal structure within the binary systems and belong thus to the methods of indirect imaging.

7.2 Disentangling of Spectra of Multiple Stars

The classical treatment of observed spectra of spectroscopic binaries consists in measuring radial velocities (RVs), $v_j|_{j=1}^n$, of the n component stars (Fig. 7.1). There are various techniques to measure RVs, but they all require some model of the component spectra, at least a simple assumption that the centres of some observed spectral lines correspond to the v_j of a particular component j. The RV curves, i.e. the set of $v_j(t)$ at different times t, are then fitted to find the orbital parameters p of the system. A simultaneous solution of other observational data such as photometry or interferometry is advantageous because these data may better constrain some of the parameters and the set of solved p may be enriched also by some more physical parameters (M, R, $T_{\rm eff}$ etc.). To relate the stellar parameters found with the spectra of individual stars, it is desirable to separate the spectrum F_j of each component j from the observed spectra F of the whole system of n components. This is possible thanks to varying conditions in the blending of components in different exposures

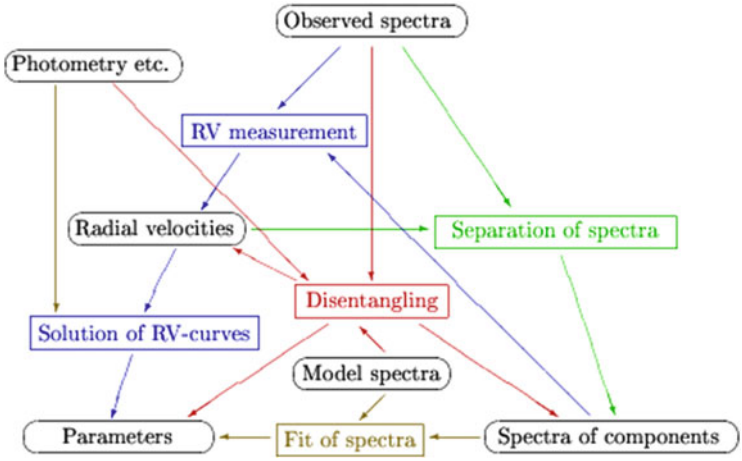

Fig. 7.1 Flow diagram of the standard data processing of spectra of multiple stellar systems and of the disentangling process

with different Doppler shifts (cf. e.g., [2]) or with different light ratios, e.g., during an eclipse (cf. [20]). The information on both the $F_j|_{j=1}^n$ and p is contained in the observed spectra, but it is entangled there because to retrieve one of them we need to know the other.

The basic idea of the method of disentangling spectra (cf. [5, 20]) is to solve simultaneously (or, actually, iteratively) the component spectra $F_j|_{j=1}^n$ and directly the orbital parameters p (instead of the intermediate step of RVs) by fitting all the observed spectra with a model of the form

$$F(x,t;p) = \sum_{j=1}^{n} F_j(x) * \Delta_j(x,t;p) \ , \tag{7.1}$$

where $x \equiv c \ln\lambda/\lambda_0$ is the logarithmic wavelength scale and the broadening function is given by a simple Doppler-shifted Dirac δ-function

$$\Delta_j(x,t;p) = \delta(x - v_j(t;p)) \ . \tag{7.2}$$

This means that the separated component spectra F_j appropriate to the observed object are also used for the treatment of RVs instead of a theoretical model or another template needed in the classical approach.

7.2.1 Fourier Disentangling

The model given by Eq. (7.1) is linear in F_j and non-linear in p. A χ^2-fit of the observed spectra with respect to $F_j(x)$ thus yields linear condition equations of the (generally large) dimension given by the number of bins of the spectra times the number of component stars. Its solution can be further simplified using the Fourier transformation $F_j(x) \rightarrow \tilde{F}_j(y)$ which converts the convolution in Eq. (7.1) into a product. The condition equation then reads

$$0 = \delta\chi^2 = \delta \sum_{l=1}^{N} \frac{1}{\sigma_l^2} \int \left| \tilde{F}(y,t_l) - \sum_{j=1}^{n} \tilde{F}_j(y)\tilde{\Delta}_j(y,t_l;p) \right|^2 dy \,, \tag{7.3}$$

where σ_l is the noise of exposure $F(x,t_l)$ obtained at time t_l and $\tilde{F}(y,t_l)$ is the y-mode of Fourier transform of $F(x,t_l)$. Variation of the right-hand side with respect to $\delta\tilde{F}_k^*(y)$ obviously yields a set of n linear equations for $\tilde{F}_j(y)$, i.e. separated subsets of equations for individual Fourier modes

$$\sum_{j=1}^{n}\sum_{l=1}^{N} \frac{\tilde{\Delta}_k^*(y,t_l;p)\tilde{\Delta}_j(y,t_l;p)}{\sigma_l^2}\tilde{F}_j(y) = \sum_{l=1}^{N} \frac{\tilde{\Delta}_k^*(y,t_l;p)\tilde{F}(y,t_l)}{\sigma_l^2} \,. \tag{7.4}$$

This makes the separation of spectra, i.e. the solution of the linear part of the disentangling, numerically easier and more efficient, compared to the solution in the wavelength domain. The optimisation with respect to δp can be then performed by numerical minimisation of the right-hand side of Eq. (7.3), e.g., using the simplex method.

It is obvious that a necessary (but not sufficient) condition to get a non-singular matrix on the left-hand side of Eq. (7.4) is $N \geq n$ and the vectors $\tilde{\Delta}_k$ should differ for at least n different t_l, i.e. the observations should sufficiently cover orbital phases with different $\tilde{\Delta}_k$. Regarding the intention to minimise the right-hand side of Eq. (7.3) with respect to p, it should be positive, i.e. Eq. (7.4) should be overdetermined and hence $N > n$. A significant over-determinacy is desirable because it can reduce the random noise in the disentangled $F_j(x)$ originating from the observational noise of $F(x,t_l)$.

For a pure orbital Doppler shift, the broadening $\Delta_j(x,t;p)$ is given by Eq. (7.2) and its Fourier transform can be calculated analytically

$$\tilde{\Delta}_j(y,t;p) = s_j(t)\exp(iyv_j(t;p)) \tag{7.5}$$

with $s_j(t) = 1$. It can be seen from here that $\tilde{\Delta}_j(y=0,t;p) = 1$ and, hence, the matrix on the left-hand side of Eq. (7.4) is singular for the zeroth Fourier mode $y = 0$. This corresponds to the obvious fact (which is also true for the separation of the spectra in the wavelength domain) that the continuum level is insensitive to

the orbital motion and consequently it cannot be disentangled from spectroscopy alone. The disentangled component spectra $F_j(x)$ are thus defined up to additive constants, the sum of which (over j) should give the mean value of all observed $F(x, t_l)$ in a particular spectral region. To get a completely separated spectra of each component like a spectrum of a single star, it is necessary to find proportions in which this sum has to be distributed between the components. This information on light ratios of the components can be in principle obtained, e.g., from interferometry (this is an example of complementarity of the direct and indirect imaging). In the case of eclipsing binaries the light ratio is usually obtained from photometry. The light ratio is wavelength dependent and is usually measured in broad wavelength regions. A normalisation of the disentangled spectra from the common continuum of the whole system to the proper continuum of each component should thus take into account the levels of continua influenced by the presence of spectral lines which are different for each component in each spectral region. Another possibility of interpretation of the disentangled spectra is to fit them by model spectra scaled in the intensity with a general unknown linear transformation.

The change of light ratio in the course of an eclipse and possibly also in other orbital phases of tidally distorted or mutually illuminated components of binaries also varies the strengths of lines of all components visible in the spectra. To get a better fit of the observed spectra in this case, line-strength factors $s_j(t)$ are introduced in Eq. (7.5) – cf. [6]. A set of linear equations for the values $s_j(t_l)|_{j=1}^{n}|_{l=1}^{N}$ can be obtained from Eq. (7.3) and solved iteratively with the separation of $F_j(x)$ – the model is bilinear in these two sets of unknown variables. The solution of s_j yields photometric information from the spectra about the luminosity of one component relative to the other one. The decrement of light due to an eclipse depends on the limb darkening which in turn depends on the source function $S_\nu(\tau_\nu)$. In the approximation of plane-parallel stellar atmosphere

$$S_\nu(\tau_\nu) = \sum_k S_{\nu,k}\tau_\nu^k \quad \Rightarrow \quad I_\nu(\tau_\nu = 0, \mu) = \sum_k S_{\nu,k}\mu^k \,, \tag{7.6}$$

which means that the dominant linear term ($k = 1$) in the dependence of the surface intensity $I_\nu \sim (1 - u + u\mu)$ on the directional cosine μ is proportional to the first derivative of S_ν with respect to the monochromatic optical depth τ_ν. In the local thermodynamic equilibrium (LTE) approximation, S_ν is given by the temperature structure of the atmosphere and $dS_\nu/d\tau_\nu$ is proportional to the vertical gradient (in geometric depth) of the temperature and inversely proportional to the monochromatic opacity. In contrary to the frequently adopted approximation that the change of limb darkening is negligible within the narrow line-profile and the value of u found from photometry (dominated by the continuum) can be fixed across the lines, u rapidly decreases from its value at the continuum toward the centre of line (cf. Fig. 7.2). Actually, the absorption lines are present in the spectra just owing to this change. In consequence, the signal contained in spectral lines normalised with respect to the overall continuum of the system may be enhanced not only for the component in foreground but also for the partly eclipsed component when only

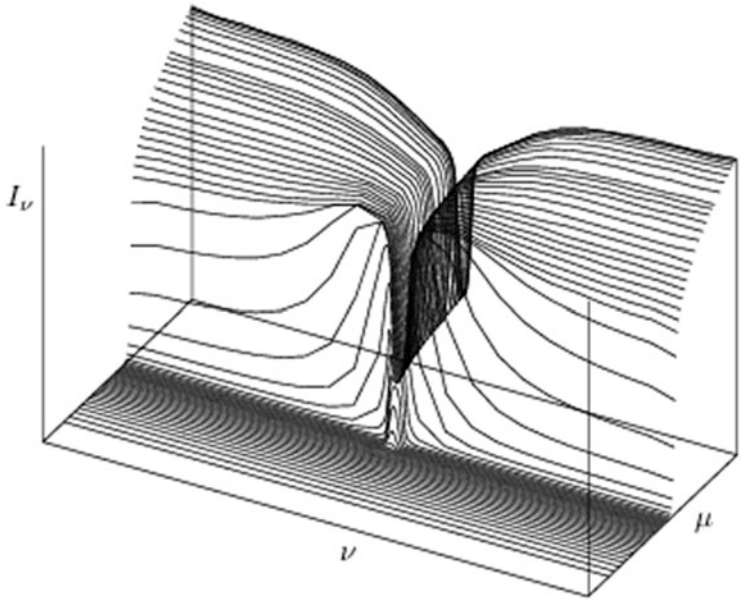

Fig. 7.2 Limb darkening within the profile of Hα line in spherical non-LTE model of stellar atmosphere ($T_{\rm eff} = 15{,}000$ K, $\log g = 2.0$; cf. [10])

an edge of its disc is eclipsed which little contributes to the line. The disentangling of the line-strength factors $s_j(t)$ thus enables to map the surface and actually also the depth structure of the eclipsed star. It may also reduce errors in rectification of the observed spectra (i.e. their normalisation with respect to the continuum), which, however, limits the information gain about the structure of the atmosphere. The line-strength factors also enable to disentangle the telluric spectrum [6, 7].

7.2.2 Generalised Disentangling

Taking into account non-LTE or higher order terms in Eq. (7.6), the spectral lines may change during an eclipse, not only in strength, but also in shape. In the approximation of a thin stellar atmosphere, the observed spectral flux $F(x,t)$ is given by an integral of the surface intensity I_j over the visible surface s of all components j,

$$F(x,t) = \sum_{j=1}^{n} \int_s \mu I_j(x,s,\mu,t) * \delta(x - v_j(s,t)) d^2 s \ , \tag{7.7}$$

where μ and v_j are known functions of s. If in analogy with Eq. (7.6) the intensity can be expressed in a form of superposition of several spectral functions F_j^k,

$$I(x, s, \mu, t) = \sum_{k=1} F_j^k(x) f_j^k(s, \mu, t) \ , \tag{7.8}$$

then the disentangling can be generalised from Eq. (7.1) to

$$F(x, t; p) = \sum_{j,k} F_j^k(x) * \Delta_j^k(x, t; p) \ , \tag{7.9}$$

where the broadening functions

$$\Delta_j^k(x, t; p) = \int_s \mu f_j^k(s, \mu, t) \delta(x - v_j(s, t)) d^2 s \tag{7.10}$$

are now dependent not only on the orbital parameters p, but also on other geometrical and physical parameters, as determined by the decomposition in Eq. (7.8).

In particular, if we treat eclipses of a rotating star, its line profile is rotationally broadened and its shape is distorted in the course of a partial eclipse. This so-called "rotational effect" [1, 8, 12, 14, 17, 18] is usually treated as a deviation of measured RVs during the eclipse from an exact Keplerian motion of the component's centres of mass. However, its value depends on the method of measurement and definition of RV of an asymmetric line-profile. The line-profiles are usually modelled in the form of Eq. (7.1), i.e. as a convolution of the profiles of a non-rotating star with a rotational broadening function. The rotational broadening, however, depends on the limb darkening – it has a semi-circular shape for a rigidly rotating sphere with uniform intensity and a parabolic shape for intensity linearly darkened to zero at the disc edge (see Fig. 7.3). As can be seen in Fig. 7.2, the line-profile generally varies across the disc (instead of a simple scaling) and, following Eq. (7.6), it should be expressed as a sum of contributions with different limb darkenings. A generalisation from Eqs. (7.1) to (7.9) for the two or more modes k of the limb darkening can thus fit the observed spectra better. The eclipse then enables to map the variations of line-profiles and hence the atmospheric structure if the quality of

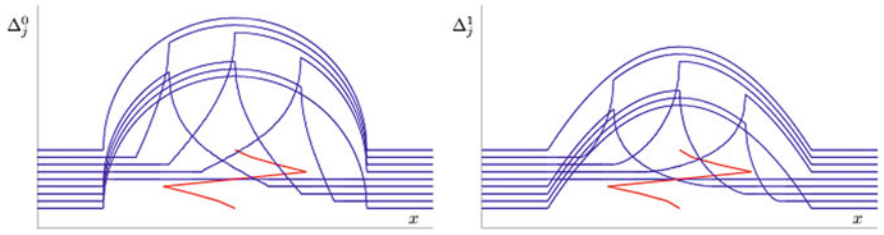

Fig. 7.3 Rotational broadening during an eclipse for $u = 0$ (*left*) and $u = 1$ (*right panel*; cf. [8])

the spectroscopic data (S/N, resolution, phase coverage) is sufficient. In addition to the synthetic spectra, more detailed results from model atmospheres are needed for interpretation of such results (as well as the other moments of $I_\nu(\mu)$). In any case, even if the data are not sufficient to distinguish between different modes k, it is preferable to fit the data with a proper model of shape of Δ_j than to modify v_j only in Eq. (7.2) because we can get a better fit of the data and more reliable parameters from the eclipse (e.g. the radii, rotational velocities or even inclinations of rotational axes, cf. [1]).

In addition to the Doppler shift according to Eq. (7.2), the broadening functions in the generalised disentangling can thus also include intrinsic variations of line profiles caused by various reasons – either geometric (e.g., eclipses, tidal distortion, spots) or physical. A frequent example of the latter case is pulsation. In the case of radial pulsations, the broadening functions for individual limb-darkening modes can be calculated explicitly (as well as their Fourier transforms, cf. [11]). This enables to disentangle directly the pulsation velocities of Cepheids and other radial pulsators and to avoid the need of the so-called projection factor which relates the effective RV measured in a particular way to the pulsation velocity. The line-strength factors $s_j(t_l)$ introduced in Eq. (7.5) as the simplest generalisation of Eq. (7.2), which are different for different lines in Cepheids depending on the influence of the temperature variations during the pulsation period on the rate of a particular transition, can reveal the temperature. In combination with photometric observations of luminosity variations or interferometric observations of changes of angular diameter, the disentangling of spectra of Cepheids may thus provide primary method of photometric or geometric determination of distance known as the Baade–Wesselink calibration of the luminosity–period relation.

7.2.3 Constrained Disentangling

As mentioned in the introduction, the aim of separating the spectra of the components is to compare them with theoretical models and to find the parameters of the component's atmospheres (cf. the "Fit of spectra" in Fig. 7.1). This comparison is usually performed by means of a least-squares fit similarly to the separation itself. Provided we have a grid of model spectra, which we believe correspond to some of the component stars, or a code for their synthesis, we can use them as template(s) by which the disentangling is constrained to a subspace of all possible solutions. The sum of the component spectra on the right-hand side of Eq. (7.1) by which we model the observed spectra $F(x,t;p)$ then generally splits into the part with the unknown component spectra $F_j(x)|_{j=1}^{m}$ (where $m < n$), which are to be disentangled and with the components constrained by templates $G_j|_{j=m+1}^{n}$ that are, however, still Doppler shifted and possibly also broadened (e.g., by some unknown rotation speed). For the

separation of F_j we thus solve a set of linear equations

$$\sum_{j=1}^{m} F_j(x) * \Delta_j(x,t;p) = F(x,t;p) - \sum_{j=m+1}^{n} G_j(x) * \Delta_j(x,t;p) \tag{7.11}$$

of the order of m only, while the template-constrained components G_j are subtracted from the observations on the right-hand side (they are the additional input to the disentangling in Fig. 7.1). The lower number of unknown spectra makes the solution less sensitive to errors on the observed data – on the other hand, the number of unknown parameters p in broadenings at both F_j and G_j usually increases a bit. For instance, the systemic velocity γ is uncertain for the standard disentangling and can only be determined when a template G_j is accepted. The line strengths of G_j are usually given relatively to the continuum level of the component j, while in the observed spectra F they are normalised by the sum of continua. Free line-strength factors s_j are thus to be solved. They reduce at the same time the uncertainty in the levels of continua discussed in Sect. 7.2.1.

As it was already mentioned and shown in Fig. 7.1, it is advantageous also in the classical approach to treat the spectroscopy together with other types of data because these may better constrain some of the parameters. The simplest way to utilise such an additional information in the disentangling is to fix the values of parameters which we know well from the other data and to converge only those, which can better be determined from the spectroscopy. However, the constraint has often the form of a hypersurface $f(p) = 0$ in the space of parameters p. For instance, the times of primary and secondary eclipses in binaries depend on the time of periastron passage, eccentricity and periastron longitude (slightly also on the inclination), but cannot determine any of these parameters unless information about some of them is available from elsewhere, e.g., from the RV-curve. The minimising of χ^2 in the p-space should thus be constrained to the hypersurface or to the cross-section of the hypersurfaces if more different constraints $f_k(p) = 0$ are given by various observations. Such a minimisation can be performed using the method of Lagrange multipliers λ_k, i.e. instead of Eq. (7.3), we minimise its more complex variant

$$0 = \delta \left\{ \sum_{l=1}^{N} \frac{1}{\sigma_l^2} \int |\tilde{F}(y,t_l) - \sum_{j=1}^{m} \tilde{F}_j(y) \tilde{\Delta}_j(y,t_l;p) - \sum_{j=m+1}^{n} \tilde{G}_j(y) \tilde{\Delta}_j(y,t_l;p)|^2 dy \right.$$
$$\left. + \sum_k \lambda_k f_k^2(p) \right\} . \tag{7.12}$$

If the constraints $f_k = 0$ are observational, they are not sharp, but due to the observational error of a probabilistic nature only. The functions $f_k^2(p)$ can thus be chosen as $(O-C)^2$, where $C = C(p)$ is a model of the observations, O, and the multipliers $\lambda_k = \sigma_k^{-2}$ are given by errors on these observations. The disentangling

thus turns into a simultaneous solution, i.e. χ^2-fitting of all available data. From the point of view of accuracy and conservation of information, it is preferable to fit the data in their original form than to reduce them into some intermediate values, such as RVs instead of the source spectra or separations and positions angles instead of visibilities for spectroscopic or interferometric binaries. On the other hand, such extracted data preserved in the literature are often the only information available, hence it is still worth to enrich, e.g., the disentangling of some spectra by simultaneous solution of RV-curves from other exposures.

7.2.4 Numerical Representation

The observed and solved spectra as well as their Fourier transforms were treated in the previous sections as continuous functions of x or y, respectively. In practice, however, the spectra are usually observed and registered using a chip with discrete pixels and represented in the data-processing from the rough data to the final separated component spectra as a finite set of values in discrete bins. It means that the space of RVs in which the spectra and the broadening functions are represented is quantised. Nevertheless, the position of a smooth line stretched over several bins can be determined with a sub-pixel resolution from asymmetry of the signal in surrounding bins. A sub-pixel resolution in RVs enables to determine the orbital parameters with a higher precision, but this, however, requires representing with a similar resolution the operator $\delta(x - v_j)$ in Eq. (7.2) or in its Fourier transform Eq. (7.5). For an integer multiple of the bin size Δ_x, the convolution with the shifted δ-function is given by multiplication with a unit off-diagonal matrix in the x-representation and by $\exp(iyv_j)$ in the y-representation, where the v_j must be rounded to the integer multiple of Δ_x to keep the periodicity in the finite set of y-values. The change of signal in a sub-pixel shift for $v < \Delta_x$ can be found from its Taylor expansion, in which its derivatives are approximated from the differences in the neighbouring bins (cf. [9]), i.e.

$$\delta(x-v) \simeq \delta(x) - \frac{v}{2\Delta_x}(\delta(x+\Delta_x) - \delta(x-\Delta_x)) + \tag{7.13}$$
$$+\frac{v^2}{2\Delta_x^2}(\delta(x+\Delta_x) - 2\delta(x) + \delta(x-\Delta_x)) + o(v^3)$$

and its Fourier transform

$$\exp(iyv_j) \simeq 1 + \frac{iv}{\Delta_x}\sin(y\Delta_x) + \frac{v^2}{\Delta_x^2}(\cos(y\Delta_x) - 1) + o(v^3)\ . \tag{7.14}$$

The Fourier disentangling with this sub-pixel resolution can be performed using the author's code KOREL, which is now available as an on-line service of the Virtual

Observatory (cf. [21]). A question frequently asked by its users is what signal-to-noise ratio (S/N) of the input spectra is needed for applicability of the method of disentangling. A general simple answer is "any, but the better is the input S/N, the better is the S/N of the disentangled component spectra and the better is the accuracy of the disentangled parameters". However, the problem is more complex. The precision of the results also depends on the degree of the overdetermination, because the noise in disentangled spectra decreases as $\sqrt{N}$ with the number N of the input spectra. But other important parameters are the spectral resolution, phase coverage and information content of the input spectra. The useful signal for disentangling are the spectral lines, i.e. deviations of the spectrum from the continuum, while the S/N compares the noise with the continuum level. To clarify this problem, a more detailed analysis is presented in the Appendix.

7.3 Disentangling of Spectra of Interacting Binaries

The method of spectra disentangling assumes that the observed system consists of several discrete sources with some general unknown spectra, the changes of which can be parameterised by means of the broadening functions Δ_j. In the case of interacting binaries with mass exchange, there is a significant contribution of radiation from the circumstellar matter continuously moving around the component stars with a complicated velocity field. The methods of Doppler tomography are used in these cases to map the distribution of the emission sources in the velocity space (cf. [13]). The intrinsic spectrum of an infinitesimal volume of the source is mostly supposed to be a Dirac δ-function in frequency at least in the vicinity of each line used for the Doppler imaging. This simplifying assumption is obviously false. (E.g., the presence of other lines or absorption features in P-Cygni profiles violate the mirror symmetry in the opposite phase supposed for the standard Doppler tomography.) It would thus be desirable to disentangle intrinsic spectra in each point of the velocity space (or even better in each point of the geometric space). This problem, however, does not have a unique solution, because a narrow line of source spread over a wide region of the velocity space results in the same spectra as a wide line from a narrow source.

Nevertheless, it is possible to approximate the smooth distribution of the circumstellar matter in the interacting binaries by several blobs of gas and to disentangle their spectra and (as a free parameter) also their positions in the velocity space. As an example, disentangling of Cyg X-1 is shown in Fig. 7.4 (cf. [22] for details). Although this source is variable on a wide range of time-scale, which violates the underlying assumptions of both the Doppler tomography as well as the disentangling, both techniques are able to reveal main features of the circumstellar matter (cf. [4, 19]).

Even in the cases when the assumptions of both these Doppler techniques are satisfied, the resolved distribution of the radiation sources in the velocity space does not yield their distribution in space and the consequent angular resolution.

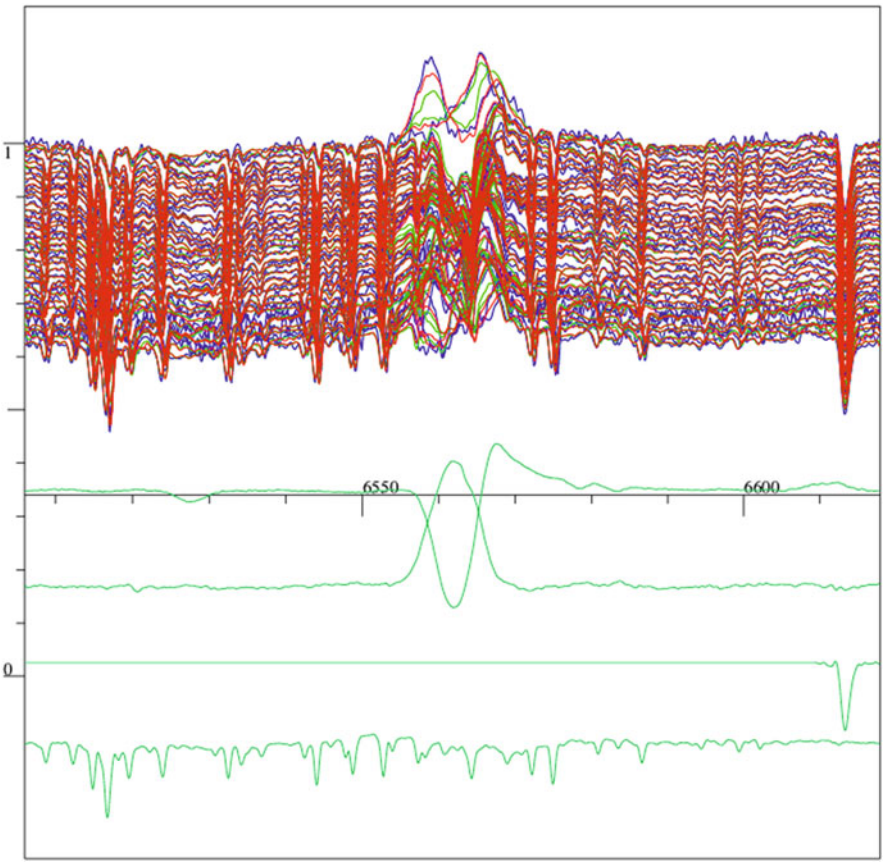

Fig. 7.4 Disentangled Hα profile of Cyg X-1. The input observed spectra (*blue lines* in the upper part of the panel) are overplotted by their reconstruction (*red lines*) from the disentangled component spectra (bottom four *green lines*): P-Cyg profile of the supergiant, emission profile of the circumstellar matter, diffuse interstellar band (the disentangled DIB is constrained by a template constant across the Hα) and telluric lines. The emission is shifted in phase with respect to the unseen black-hole secondary and its strength is anti-correlated with the X-ray emission

Generally there is no one-to-one correspondence between these spaces due to the non-uniformity of the velocity field. To get an information about the spatial structure of the source, the interpretation must be constrained by an appropriate theoretical model (based e.g. on radiation hydrodynamics, cf. [3]) of the source and its radiation. The method of synthetic Dopplerograms is promising for this purpose (cf. [4, 16]).

A direct comparison of the observations with synthetic spectra based on sophisticated models of the sources may be more precise because it may avoid discrepancies caused by the simplifying assumptions of the methods of indirect imaging. However, these techniques are useful for indicating the dominant features in the observed

phenomena and their achievements as well as failures are intuitive in suggesting the way in which the theory should proceed.

Acknowledgements This work has been supported by the Czech Science Foundation (GAČR 14-37086G) – Albert Einstein Center for Gravitation and Astrophysics.

Appendix: Bayesian Estimation of Parameters Errors

The errors of parameters of a stellar system determined by disentangling of spectra can be estimated using Bayesian statistics. The errors are caused mainly by the noise in the observed spectra but they are also influenced by the phase distribution of the observations and by the sensitivity of the available data to a particular parameter. Usually we "know" in advance only that the values of parameters p can be expected in some "reasonable" regions (e.g., hundreds of km/s for orbital RVs, days or from hours to months for the orbital period, the line strengths and widths corresponding to the spectral types and rotational broadening, etc.). If previous studies of the same system exist their results can be taken as a more specific limitation of the possible range of p (and a first estimate of the new solution), which we want to verify or improve using a set of new data. If the old data are available they can be included together with the new ones into the new solution, otherwise the reliability of the old results must be estimated and they can be included into the new solution as constraints to the solution in the space of parameters p. Having the set of new observations, i.e. the spectra $F(x)$, we can find the "posterior" probability $P(p|F)$ of p agreeing with the new data according to Bayes' theorem

$$P(p|F) = \frac{P(F|p)P(p)}{P(F)} , \tag{7.15}$$

where $P(p)$ is the "prior" probability of p (i.e. either a smooth characteristic of the wide range of "reasonable" values or the constraint resulting from the old data), $P(F|p)$ is the "liability" that for a chosen value of p the particular shape of $F(x)$ will be detected and $P(F)$ is a general probability do detect the signal $F(x)$. The best new solution $p_{\max}$ can be then defined as the maximum of $P(p|F)$ in the p-space or we can find a mean value

$$\langle p \rangle = \int pP(p|F)dp \tag{7.16}$$

(if $P(p|F)$ is normalised to unity, i.e., $\int P(p|F)dp = 1$). In both cases the result depends on our choice of measures in the p space. The errors of resulting parameters p can be estimated from the behaviour of $P(p|F)$ around the found solution. Because p is generally multidimensional (and different dimensions can be of different nature), it is not sufficient to attribute some error bar to each component

of p separately as it is a common habit. If $P(p|F)$ is sufficiently smooth around its maximum, it can be expanded into a Taylor series up to quadratic terms in variation of δp and the non-diagonal components of the corresponding quadratic form determine the correlation of the parameters. Generally, however, there may be several local maxima in the p-space, which may be treated as different solutions.[1] The errors of these different solutions must be then determined from a local behaviour of $P(p|F)$. Generally, the information about the studied system is more completely characterised by mapping of $P(p|F)$ than by a simple list of found values of p and their errors.

Errors of Line Strengths and Radial Velocities

We shall illustrate the calculation of $P(p|F)$ first on a toy model of measurements of one spectrum of a single star. Let us assume that the observed spectrum $F(x)$ is given by

$$F(x) = f(x,p) + \delta F(x) \,, \tag{7.17}$$

where $\delta F(x)$ is a random observational noise. We fit $F(x)$ by a model $f(x,p)$ dependent on a parameter (or a set of parameters) p by minimising the residual error

$$S(p) = \int_D (F(x) - f(x,p))^2 dx \tag{7.18}$$

integrated over the whole observed region D of x. The equation(s) for p thus reads

$$0 = \frac{\partial S(p)}{\partial p} = 2 \int \frac{\partial f(x,p)}{\partial p} (f(x,p) - F(x)) dx \,. \tag{7.19}$$

The random fluctuations δF in the observed signal $F(x)$ blur this condition and result in a deviation δp of the solution from its correct value. These variations are related by the condition

$$\delta p \frac{\partial}{\partial p} \int \frac{\partial f(x,p)}{\partial p} (f(x,p) - F(x)) dx = \int \frac{\partial f(x,p)}{\partial p} \delta F(x) dx \,. \tag{7.20}$$

[1] A typical example is the epoch of a periodic RV curve, where for each solution there is an infinite set of solutions differing by an integer multiple of the period. These solutions are usually taken as equivalent. The errors and correlation of the epoch with the period depend on which of these solutions we choose. The period itself may have several solutions due to aliasing in quasi-periodically sampled data or due to an interference of data obtained in two time-remote observational seasons.

For example, let the spectrum be rectified, i.e. normalised to the continuum, which means $f = 1 - \varphi$, where $\varphi(x)$ corresponds to the spectral lines. We shall assume first that the only unknown free parameter p is the strength of lines, i.e., the model has the form

$$f(x,p) = 1 - p\varphi_1(x) \ , \tag{7.21}$$

where φ_1 is a pattern of the line-profile(s) imprinted into the observed spectrum $F(x)$ with an unknown amplitude (e.g., due to uncertainty in element abundances, due to a contamination of the signal by light of another star or due to instrumental error in subtracting dark signal). Equation (7.19) is then a simple linear equation with solution

$$p = \frac{\int (1 - F(x))\varphi_1(x)dx}{\int \varphi_1^2(x)dx} \tag{7.22}$$

and in agreement with Eq. (7.20) its variations are given by

$$\delta p = -\frac{\int \varphi_1(x)\delta F(x)dx}{\int \varphi_1^2(x)dx} \ . \tag{7.23}$$

The integrals in these equations are actually summations over K individual pixels (each one of size $\Delta_x = D/K$) in real observations,

$$\int \varphi_1(x)\delta F(x)dx = \Delta_x \sum_{i=1}^{K} \varphi_1(x_i)\delta F(x_i) \ , \tag{7.24}$$

$$\int \varphi_1^2(x)dx = \Delta_x \sum_{i=1}^{K} \varphi_1^2(x_i) \ . \tag{7.25}$$

Let us assume that the probability distribution of the noise δF of the signal $F(x)$ in each pixel can be approximated as a Gaussian with standard deviation σ, i.e., the probability of its value δF in one pixel x_i is

$$P(\delta F(x_i)) \simeq \exp(-\frac{\delta F(x_i)^2}{2\sigma^2}) \tag{7.26}$$

and, hence, the statistical mean value is $\langle \delta F^2 \rangle = \sigma^2$. In addition, the noise in different pixels is supposed to be statistically independent, i.e.,

$$\langle \delta F(x_i)\delta F(x_j) \rangle = \sigma^2 \delta_{ij} \ . \tag{7.27}$$

The probability distribution of error δp is then also Gaussian[2] with

$$\langle \delta p^2 \rangle = \frac{\Delta_x^2}{\left[\int \varphi_1^2(x)dx\right]^2} \langle [\sum_{i=1}^{K} \varphi_1(x_i)\delta F(x_i)]^2 \rangle = \frac{\Delta_x \sigma^2}{\int \varphi_1^2(x)dx} \,. \tag{7.28}$$

The squared error of p thus decreases inversely proportionally with the number of pixels covering the profile $\varphi(x)$. It can be seen from Eqs. (7.22) and (7.23) that the strength p and its uncertainty δp are predominantly determined by the parts of the spectrum where the lines φ_1 of the model are deep.

If the unknown free parameter p is the Doppler shift of the spectrum, the model has the form

$$f(x) = 1 - \varphi_0(x - p) \,, \tag{7.29}$$

where $\varphi_0(x)$ is a model line-profile in laboratory wavelength scale. The residual noise

$$S(p) = \int (\varphi_0(x - p) - \varphi(x) + \delta F(x))^2 dx \tag{7.30}$$

is then no more a simple quadratic function of p and Eq. (7.19), which reads now

$$0 = \frac{\partial S(p)}{\partial p} = -2 \int \frac{d\varphi_0(x-p)}{dx} (\varphi_0(x - p) - \varphi(x) + \delta F(x))dx, \tag{7.31}$$

may have several solutions for p corresponding to coincidences of some improperly identified observed lines with wrong lines in the model. The uncertainty of p in each of these solutions can be estimated from the depth and width of the local minimum of the residual noise. Equation (7.20) reads now

$$\delta p \int \left(\frac{d\varphi_0}{dx}\right)^2 dx = \int \frac{d\varphi_0}{dx} \delta F(x)dx \,, \tag{7.32}$$

where we have skipped the term $\frac{d^2\varphi_0}{dx^2}(\varphi_0 - \varphi)$ which should vanish at the correct value $p = p_0$ where $\varphi = \varphi_0$ (this need not be true at a false minimum). This equation shows that the error δp of RV is dominated by the noise δF in the steepest parts of the line profile. Analogously to Eq. (7.28), the mean squared value of this

[2] If a quantity x has a probability distribution $\exp(-(x - x_0)^2/(2\alpha^2))$ and quantity y a distribution $\exp(-(y - y_0)^2/(2\beta^2))$ then the linear combination $ax + by$ has a mean value $\langle ax + by \rangle = ax_0 + by_0$ and the quadratic error $\langle (a(x - x_0) + b(y - y_0))^2 \rangle = a^2\alpha^2 + b^2\beta^2$. Similarly for a sum of more statistically independent quantities we get recursively $\langle \sum_{i=1}^{n} a_i x_i \rangle = \sum_{i=1}^{n} a_i x_{i0}$ and $\langle (\sum_{i=1}^{n} a_i (x_i - x_{i0}))^2 \rangle = \sum_{i=1}^{n} a_i^2 \alpha_i^2$.

error is now

$$\langle \delta p^2 \rangle = \frac{\Delta_x \sigma^2}{\int (\frac{d\varphi_0}{dx})^2 dx} \,. \tag{7.33}$$

The difference between Eqs. (7.28) and (7.33) is due to the fact that the fit of line strengths is most sensitive to the part of the spectrum where the line is deepest, while the Doppler shift is most sensitive to the wings where the line profile is steepest.

Errors in Multidimensional Space of Parameters

We can optimise the fit of the observed spectrum simultaneously with respect to the line-strength, Doppler shift and some additional parameters. Generally, if the model spectrum $\varphi_0(x, p)$ is a function of several parameters $p_i|_{i=1}^m$, we get for them a set of m generally non-linear equations for p

$$0 = \int \frac{\partial \varphi_0}{\partial p_i} (1 - F(x) - \varphi_0(x, p)) dx \,. \tag{7.34}$$

Linearising, we arrive at the set of equations

$$M_{ij} \delta p_j = \delta R_i \tag{7.35}$$

for variations δp_j caused by variations $\delta F(x)$ of the observed spectrum. The matrix M_{ij} is given here by

$$M_{ij} \equiv \int \left(\frac{\partial \varphi_0}{\partial p_i} \frac{\partial \varphi_0}{\partial p_j} - \frac{\partial^2 \varphi_0}{\partial p_i \partial p_j} (1 - F(x) - \varphi_0(x, p)) \right) dx \tag{7.36}$$

and the right-hand side by

$$\delta R_i \equiv - \int \frac{\partial \varphi_0}{\partial p_i} \delta F(x) dx = \Delta_x \sum_{k=1}^{K} \frac{\partial \varphi_0(x_k)}{\partial p_i} \delta F(x_k) \,. \tag{7.37}$$

Depending on the form of the model φ_0, some variation δF can be compensated by a change of different p_i, so that their variations may be correlated

$$\langle \delta p_j \delta p_k \rangle = M_{ji}^{-1} M_{kl}^{-1} \langle \delta R_i \delta R_l \rangle \,. \tag{7.38}$$

Assuming that the noise $\delta F(x)$ is statistically independent at different pixels x_k, x_l, we have

$$\langle \delta R_i \delta R_l \rangle = \Delta_x^2 \sum_{k,l=1}^{K} \frac{\partial \varphi_0(x_k)}{\partial p_i} \frac{\partial \varphi_0(x_l)}{\partial p_j} \langle \delta F(x_k) \delta F(x_l) \rangle = \\ = \Delta_x \int \frac{\partial \varphi_0}{\partial p_i} \frac{\partial \varphi_0}{\partial p_j} \langle \delta F(x)^2 \rangle dx \, . \tag{7.39}$$

If the noise $\langle \delta F(x)^2 \rangle = \sigma^2$ is statistically the same in all pixels and if the second term in the integral in Eq. (7.36) is negligible compared to the first one (which is the case if the fit is good and $F(x) \simeq 1 - \varphi_0(x, p)$), then

$$\langle \delta R_i \delta R_l \rangle = \Delta_x \sigma^2 M_{il} \tag{7.40}$$

and

$$\langle \delta p_j \delta p_k \rangle = \Delta_x \sigma^2 M_{jk}^{-1} \, . \tag{7.41}$$

As an example, let us investigate a fit by a simple Gaussian profile

$$f(x, p) = 1 - \varphi_0(x, p) = 1 - p_1 \exp\left(-\frac{(x - p_3)^2}{p_2^2} \right) \, . \tag{7.42}$$

Equation (7.34) then reads

$$0 = \int (x - p_3)^k \varphi_0 (1 - F - \varphi_0) dx \, , \tag{7.43}$$

where $k = 0, 2, 1$ in conditions for p_1, p_2, p_3, resp. The variation of φ_0 reads

$$\delta \varphi_0 = \left(\frac{1}{p_1} \delta p_1 + 2 \frac{(x - p_3)^2}{p_2^3} \delta p_2 + 2 \frac{x - p_3}{p_2^2} \delta p_3 \right) \varphi_0 \, , \tag{7.44}$$

so that neglecting the second term in Eq. (7.36), the matrix M has the form

$$M_{ij} \simeq \int \frac{\partial \varphi_0}{\partial p_i} \frac{\partial \varphi_0}{\partial p_j} dx = \sqrt{\frac{\pi}{2}} \begin{pmatrix} p_2 & \frac{p_1}{2} & 0 \\ \frac{p_1}{2} & \frac{3p_1^2}{4p_2} & 0 \\ 0 & 0 & \frac{p_1^2}{p_2} \end{pmatrix} \tag{7.45}$$

and hence according to Eq. (7.41) the correlation matrix of parameter errors reads

$$\langle \delta p_j \delta p_k \rangle \simeq \sqrt{\frac{2}{\pi}} \Delta_x \sigma^2 \begin{pmatrix} \frac{3}{2p_2} & -\frac{1}{p_1} & 0 \\ -\frac{1}{p_1} & \frac{2p_2}{p_1^2} & 0 \\ 0 & 0 & \frac{p_2}{p_1^2} \end{pmatrix} . \tag{7.46}$$

It means that the errors of the depth p_1 and the width p_2 of the line-profile given by Eq. (7.42), which are due to the part of the perturbation δF symmetric with respect to the centre of the line, are anti-correlated, while the error in the position p_3 of the line centre is not correlated with them and its squared value is half of that of the width.

Results of a Monte Carlo simulation of this example can be seen in Fig. 7.5. The red line shows the profile (cf. Eq. (7.42)) for $p_1 = 0.2$, $p_2 = 0.2$ and $p_3 = 0.0$. The black line has added a randomly generated noise with $\sigma = 0.04$ in 1024 pixels in the displayed interval of $x \in (-1, +1)$, i.e., $\Delta_x = 2^{-9} \simeq 0.00195$. The blue line gives the best fit to this particular simulated measurement, which was found for values of parameters $p_1 \simeq 0.2002$, $p_2 \simeq 0.2085$ and $p_3 = 0.0029$. The figure included in the bottom left corner shows the scatter of p_1 and p_2 around their true values for 1000 different choices of δF (the drawn parts of coordinates correspond to ± 0.01). Similarly the histogram in the right corner shows the distribution of p_3 (the width of each histogram column is 0.001). If the noise σ is decreased then

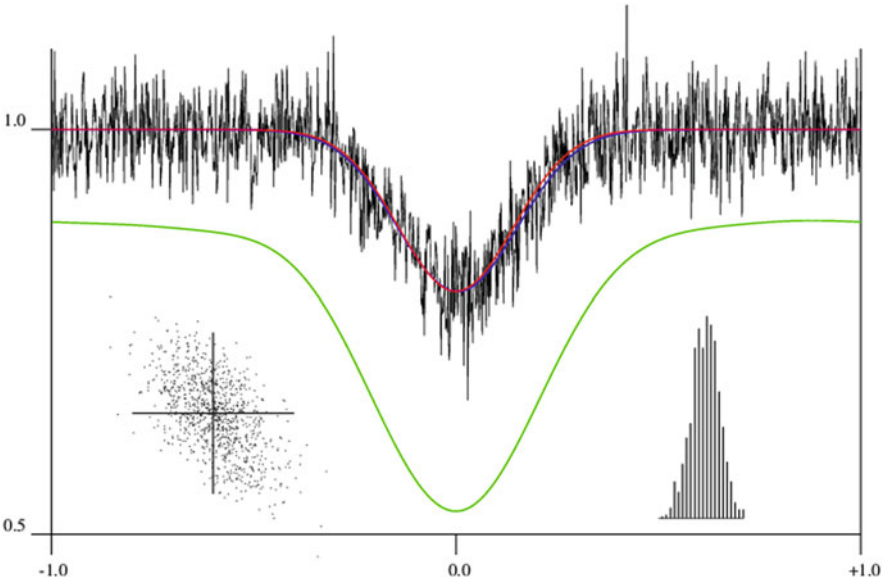

Fig. 7.5 Gaussian line-profile (*red line*) with a simulated noise (*black line*) and its best fit (*blue line*; see text for a detailed description)

in agreement with Eq. (7.38) or its approximation (Eq. (7.41)) also the uncertainty $\langle \delta p_j \delta p_k \rangle$ of the parameters p is reduced. This agrees with the Bayes theorem (Eq. (7.15)) according to which the probability $P(p|F)$ of a larger difference of the true value of p from its best fit to particular data $F(x)$ decreases with decreasing probability $P(F|p)$ that the random noise will mimic a wrong spectrum.

For real observed spectra we do not know the exact value of σ (which can only be estimated from the level of signal integrated during the exposure), while we may have a rough estimate only of Δ_x and, generally, we do not know the explicit form of the matrix M_{ij} and its inversion. However, we can estimate these values from the value S_0 of the residuum $S(p)$ in its minimum and from variations of $S(p)$ with respect to variations of p. If the spectrum is correctly fitted by a proper model, the residuum S_0 should be given by the noise[3] only, i.e.,

$$S_0 \simeq \int \delta F^2(x) dx = D\sigma^2 = K\Delta_x \sigma^2 \,. \tag{7.47}$$

The value of Δ_x and hence for known D also the number K of statistically independent pixels of noise can be estimated from auto-correlation of the residual noise. In our example, the numerical simulation results in $S_0/\Delta_x \simeq 1.73$, giving $\sigma \simeq 0.0411$ in good agreement with the value 0.04 for which the noise was generated. The residuum $S(p_3)$ is drawn by the green line in Fig. 7.5 as a function of p_3 for $p_{1,2}$ fixed to their best values (the zero level is shifted to the bottom of the panel for $S(p_3)$). Its behaviour can be estimated substituting φ_0 from Eqs. (7.42) into (7.30) also for φ,

$$\begin{aligned} S(p_3) &\simeq \int (\varphi_0(x-p_3) - \varphi_0(x) + \delta F(x))^2 dx \\ &\simeq \int \delta F^2(x) dx + \int \varphi_0^2(x) dx + \int \varphi_0^2(x-p_3) dx - 2\int \varphi_0(x-p_3)\varphi_0(x) dx \\ &= S_0 + \sqrt{2\pi} p_1^2 p_2 \left(1 - \exp(-\frac{p_3^2}{2p_2^2})\right) \,. \end{aligned} \tag{7.48}$$

The residual $S(p_3)$ thus increases with the square of δp_3 around its minimum

$$S(\delta p_3) \simeq S_0 + \sqrt{\frac{\pi}{2}} \frac{p_1^2}{p_2} \delta p_3^2 \,, \tag{7.49}$$

but it approaches saturation at level $S_\infty = S_0 + \sqrt{2\pi} p_1^2 p_2$ for large δp_3 (in agreement with numerical results $S_\infty/\Delta_x \simeq 12.5$ in our example). This saturation corresponds

[3] In the discrete representation of N input spectra, the residual noise after disentangling of m components is given by the sum $S_0 \simeq (N-m)K\sigma^2$. However, it should be noted that both the signal and its noise may be rescaled by the Fourier transform and hence (due to the use of FFT) the residuum on output from KOREL is KS_0.

to the possibility that the line visible in the spectrum is actually a random fluctuation of the noise, while the real line is in the distant wavelength δp_3, but it is hidden in another noise fluctuation. The probability of this "hidden" solution is proportional to the width D of the wavelength interval. This may be in principle infinite, so that the probability of this solution may be high, even for a small value of σ. The limitation of D to the interval $(-1, +1)$ in our example has a character of the prior $P(p_3)$ which is chosen equal to zero out of this interval.

Regarding the assumption of the Gaussian noise (7.26), the liability $P(\delta F|p)$ of the noise $\delta F(x_i)|_{i=1}^{K}$ in all pixels is

$$P(\delta F|p) \simeq \exp\left(-\frac{\sum_i \delta F(x_i)^2}{2\sigma^2}\right) = \exp\left(-\frac{S_0}{2\Delta_x \sigma^2}\right) . \tag{7.50}$$

Following Bayes' theorem (Eq. (7.15)), the probability of p for known F (and a 'flat' prior $P(p)$) reads

$$P(p|F) \simeq \exp\left(-\frac{S(p)}{2\Delta_x \sigma^2}\right) \simeq \exp\left(-\frac{KS(p)}{2S_0}\right) . \tag{7.51}$$

We thus obtain from Eq. (7.49) the probability distribution of radial velocity δp_3 of the "visible" line

$$P(\delta p_3|F) \simeq \exp\left(-\frac{KS(\delta p_3)}{2S_0}\right) \sim \exp\left(-\sqrt{\frac{\pi}{2}}\frac{p_1^2}{2\Delta_x \sigma^2 p_2}\right), \tag{7.52}$$

which yields, according to the definition (Eq. (7.16)), a mean value of squared velocity shift

$$\langle \delta p_3^2 \rangle = \frac{\int \delta p_3^2 P(\delta p_3|F) d\delta p_3}{\int P(\delta p_3|F) d\delta p_3} \simeq \sqrt{\frac{2}{\pi}}\frac{\Delta_x \sigma^2 p_2}{p_1^2}, \tag{7.53}$$

in agreement with component $\{j, k\} = \{3, 3\}$ of Eq. (7.46).

It is worth noting that the error $\sqrt{\langle \delta p_3^2 \rangle}$ on the radial velocity p_3 is proportional to the ratio σ/p_1 of the noise to the line depth. Regarding the problem of desirable S/N-ratio mentioned in Sect. 7.2.4, we can see from this relation that there is no limitation. However, the higher the S/N-ratio is, the more precise is the determination of the disentangled parameters. From the observational and instrumental point of views, the S/N of spectra refers to the ratio of the noise to the overall spectral flux, i.e. the signal means the continuum. However, it is obvious that the signal which yields an information about RV and other spectral features is the modulation of the flux by spectral lines. It is thus desirable to optimise in the observations the ratio of line depths to the (photon) noise. The RV error is also proportional to the square root of the line width p_2 which indicates that a higher precision can be achieved

from sharper lines, although they are covered by smaller number of pixels and are thus more influenced by fluctuations in photon counts.

In the disentangling technique, we do not have explicitly given in Eq. (7.17) the template spectrum $f(x,p)$, like in Eqs. (7.21) or (7.42), but a more complicated expression like the right-hand side of Eqs. (7.1) or (7.9). The component spectra $F_j(x)$ whose imprints we want to find in the observations are now also unknown parameters that can be retrieved with some errors only. In analogy to Eq. (7.28), this error is proportional to the noise σ of the input spectra. However, usually the separation of the component spectra is overdetermined, as explained in Sect. 7.2.1 and hence, following the relations in the Footnote 2, the amplitude of the noise of the disentangled spectra decreases inversely proportionally to the square root of the number of observed spectra. The dependence of the model $f(x,p)$ on nonlinear parameters p in the broadening functions $\Delta_j(x,t;p)$ is more complicated and generally cannot be expressed explicitly like in the above given toy models. However, it is possible to map the distribution of the residual noise numerically as a function of these parameters.

References

1. Albrecht, S.: The long history of the Rossiter – McLaughlin effect and its recent applications. IAUS **282**, 379–384 (2012)
2. Bagnuolo, W.G., Jr., Gies, D.R.: Tomographic separation of composite spectra – the components of the O-star spectroscopic binary AO cassiopeiae. ApJ **376**, 266–271 (1991)
3. Čechura, J., Hadrava, P.: Stellar wind in state transitions of high-mass X-ray binaries. A&A **575**, A5 (2015)
4. Čechura, J., Vrtilek, S.D., Hadrava, P.: Interpreting the X-ray state transitions of Cygnus X-1. MNRAS **450**, 2410–2422 (2015)
5. Hadrava, P.: Orbital elements of multiple spectroscopic stars. A&AS **114**, 393–396 (1995)
6. Hadrava, P.: Relative line photometry of eclipsing binaries. A&AS **122**, 581–584 (1997)
7. Hadrava, P.: Disentangling telluric lines in stellar spectra. A&A **448**, 1149–1152 (2006)
8. Hadrava, P.: Line profiles during eclipses of binary stars. ASPC **370**, 164–168 (2007)
9. Hadrava, P.: Notes on the disentangling of spectra. I. Enhancement in precision. A&A **494**, 399–402 (2009)
10. Hadrava, P., Kubát, J.: Limb darkening and line-profile variations in eclipsing binaries. ASPC **288**, 149–152 (2003)
11. Hadrava, P., Šlechta, M., Škoda, P.: Notes on disentangling of spectra. II. Intrinsic line-profile variability due to cepheid pulsations. A&A **507**, 397–404 (2009)
12. Holt, R.J.: Spectroscopic determination of stellar rotation. Astron. Astro-Phys. **12**, 646 (1893)
13. Marsh, T.R., Horne, K.: Images of accretion discs. II – Doppler tomography. MNRAS **235**, 269–286 (1988)
14. McLaughlin, D.B.: Some results of a spectrographic study of the Algol system. ApJ **60**, 22–31 (1924)
15. Ribas, I., Jordi, C., Vilardell, F., et al.: First determination of the distance and fundamental properties of an eclipsing binary in the andromeda galaxy. ApJ **635**, L37–L40 (2005)
16. Richards, M.T., Cocking, A.S., Fisher, J.G., et al.: Images of gravitational and magnetic phenomena derived from two-dimensional back-projection Doppler tomography of interacting binary stars. ApJ **795**, 160 (2014)

17. Rossiter, R.A.: On the detection of an effect of rotation during eclipse in the velocity of the brigher component of beta Lyrae, and on the constancy of velocity of this system. ApJ **60**, 15–21 (1924)
18. Schlesinger, F.: The Algol-variable δ Librae. Publ. Allegh. Obs. **1**, 123–134 (1910)
19. Sharova, O.I., Agafonov, M.I., Karitskaya, E.A., et al.: Doppler tomography in 2D and 3D of the X-ray binary Cyg X-1 for June 2007. IAUS **282**, 201–202 (2012)
20. Simon, K.P., Sturm, E.: Disentangling of composite spectra. A&A **281**, 286 (1994)
21. Škoda, P., Hadrava, P.: Fourier disentangling using the technology of virtual observatory. ASPC **435**, 71–75 (2010)
22. Yan, J.Z., Liu, Q.Z., Hadrava, P.: Optical spectroscopic observations of Cyg X-1 = HDE 226868. AJ **136**, 631–640 (2008)
23. Zwahlen, N., North, P., Debernardi, Y., et al.: A purely geometric distance to the binary star Atlas, a member of the Pleiades. A&A **425**, L45–L48 (2004)